Controlling Couette flow by alternating axial mass flux

Sebastian A. Altmeyer[1, a)]
Castelldefels School of Telecom and Aerospace Engineering, Universitat Politècnica de Catalunya, 08034 Barcelona, Spain

(*Electronic mail: sebastian.andreas.altmeyer@upc.edu.)

(Dated: 24 April 2024)

This paper presents numerical simulations of the Taylor vortex flow (TVF) under the influence of an externally applied alternating axial mass flux (through-flow) in a Taylor-Couette system with axial periodic boundary conditions. Such an axially modulating flow can lead to a significant variation in the onset of primary instabilities. Depending on the system parameters, the effect can be both stabilizing and destabilizing – that is shifting the bifurcation threshold to larger or smaller control parameters, respectively. It is found that the system response around the primary instability is sensitive to and critically influenced by an alternating mass flux, particularly the modulation frequency. We show that such an alternating axial flow represents an easily and, more importantly, precisely controllable key parameter to change the non-linear system response from subcritical to supercritical behavior and vice versa. Furthermore, we observe different parameter regimes with regular and irregular intermittent flow dynamics.

I. INTRODUCTION

Since the seminal work of G. I. Taylor[1], the flow in the gap between two concentric, independently rotating cylinders – that is, the Taylor-Couette flow – has been the subject of numerous intensive theoretical, numerical, and experimental investigations and has led to a deeper understanding of fundamental hydrodynamic concepts and stabilities[1,2]. The superposition of the basic circular Couette flow (CCF) and a pressure-driven axial flow in an annulus leads to a configuration in which two mechanisms for instability are present. Here, the centrifugal instability, which is based on the curved streamlines of the CCF, competes with the shear instability, which is based on the axial flow.

This study is primarily driven by the several essential engineering and technological uses of such a system setup – a pressure-driven axial mass flux in an annulus between rotating cylinders. Apart from traditional aspects in centrifugal extractors[11], and biological reactors[12], key applications range from rotating filtration of suspensions and water treatment by reverse osmosis[3–7] to medical use for blood filtration[8–10].

Almost all research thus far on the *Taylor-Couette flow* has focused on axial through-flow and has only examined the *static* (time-independent) case of continuous axial mass flux[13–17]. Based on Taylor's work[1], numerous impacts of such externally induced flow have been studied throughout the last century. The list is far too long to be completely constituted here". These works include the linear analysis of the competition between the two competing instabilities – shear and centrifugal stability mechanisms[19,20]; the linear analysis of Taylor vortex flow (TVF) and spiral vortex flow (spirals, SPI) fronts and pulses[21,22]; weakly nonlinear bifurcation analysis[16,18] of axially extended spiral, ribbon, and mixed vortex states with homogeneous amplitudes[2,23]; and experimental measurements of velocity fields by particle image velocimetry[17]. Numerous other theoretical and numerical investigations have focused on non-linear pattern selection in the absolutely unstable regime under downstream evolving intensity envelopes[24], the effect of thermal noise[25,26], and on studies of the changes in behavior around and across the convective-absolute stability boundary[15,22,27].

All the aforementioned research reaches the same conclusion, which is that the system's stability is altered when an axial flow is added to the annulus. Depending on the characteristics and flow configurations involved, there is either stabilization or destabilization[14] of the CCF's fundamental state. Consequently, changes are made to the crucial Reynolds number, wavelength, and vortex shape in addition to the fundamental bifurcating thresholds. Depending on the parameter values, the dominant bifurcating flow state can alternate between SPI[14,22,28] and TVF, with the latter being preferred as axial flow increases. More recently, research has also been conducted on more complex fluids with axial mass flux[29,30].

With knowledge of the effect of a static applied mass flux, the question that arises is how the system reacts to periodic forcing. A periodically modulated, externally applied axial mass flux is one way to introduce such a driving force into the system. This leads to a time-dependent axial Reynolds number $Re(t)$. In the present study, we investigate such an alternating axial flow with specific attention to the control parameters around the bifurcation threshold of the primary instability. Understanding the evolving dynamics and response of the system as it moves along the edge of instability between sub- and supercritical states is a major focus of the present study. The effects of alternating axial through-flow and the resultant interactions and changes in the hydrodynamics are investigated. The variations in modulation frequency Ω_{Re} and amplitude result in a significant change in system stability. We illustrate that such an alternating axial flow leads to intermittent behavior between supercritical and subcritical flow dynamics, while this intermittency can be either regular or irregular. In conclusion, such a setup may provide a *simple* and *accurate* means to balance the system to be operated subcritically, supercritically, or intermittently.

[a)]http://www.sebastianaltmeyer.de.

II. MATERIALS AND METHODS

A. Governing equations

We consider the Taylor-Couette flow[1,2] – the flow driven in an annular gap between two independently rotating cylinders, where the inner cylinder of radius R_i rotates at angular velocity ω_i and the outer cylinder of radius R_o is at rest. In the present study, we utilize axial periodic boundary conditions, which are set to $\lambda/(R_o - R_i) = 1.6$ (λ is the axial wavelength) – that correspond to an axial wavenumber $k = (2\pi/\lambda) = 3.927$. The fluid in the annulus is assumed to be Newtonian, isothermal, and incompressible with kinematic viscosity, ν. The non-dimensional Navier-Stokes equations that govern the flow are

$$\partial_t \mathbf{u} + (\mathbf{u}\cdot\nabla)\mathbf{u} = -\nabla p + \nabla^2 \mathbf{u}, \qquad \nabla\cdot\mathbf{u} = 0, \tag{1}$$

where $\mathbf{u} = (u, v, w)$ is the velocity in cylindrical coordinates (r, θ, z) and the corresponding vorticity is $\nabla\times\mathbf{u} = (\xi, \eta, \zeta)$. The system is governed by the following independent non-dimensional parameters: the inner Reynolds number (the ratio between inertia and viscous forces): $\mathrm{Re_i} = \omega_i R_i d/\nu$, the axial Reynolds number: $Re = \langle w_{\mathrm{APF}}(r,t)\rangle$ (see below), and the radius ratio: $b = R_i/R_o$. In this study, a fixed wide-gap radius ratio $b = 0.5$ is used and length and time scales of the system are set by the gap width $d = R_o - R_i$ and the diffusion time d^2/ν, respectively. The pressure in the fluid is normalized by $\rho\nu^2/d^2$. Further, boundary conditions on the cylindrical surfaces are $\mathbf{u}(r_i, \theta, z, t) = (0, \mathrm{Re_i}, 0)$ and $\mathbf{u}(r_o, \theta, z, t) = (0, 0, 0)$, with the non-dimensional inner [outer] radius $r_{i[o]} = R_{i[o]}/d$.

B. External axial through-flow Re

The external axial mass flux in the annulus is forced by a time-dependent external pressure gradient with the magnitude

$$\partial_z p_{\mathrm{APF}}(t) = \partial_z[p_{S,\mathrm{APF}} + p_{M,\mathrm{APF}} \sin(\Omega_{Re} t)] \tag{2}$$

to the axial velocity component in the Navier-Stokes equations (Eq. (1)). In the subcritical region (below the onset of any vortex structure), this pressure gradient forces an annular Poiseuille flow (APF)[31,32]. The radial profile of this axial flow velocity is given by

$$w_{\mathrm{APF}}(r,t) = \frac{\partial_z p_{\mathrm{APF}}(t)}{4}\left[r^2 + \frac{(1+b)\ln r}{(1-b)\ln b} + \frac{(1+b)\ln(1-b)}{(1-b)\ln b} - \frac{1}{(1-b)^2}\right]. \tag{3}$$

The analytical solution (Eq. (3)) was checked to be reproduced by our numerical code. The radial mean values $\langle\cdot\rangle_r$ of the static and modulated contribution can be used to define the time-dependent axial flow Reynolds number:

$$\begin{aligned} Re(t) :=& \quad \langle w_{\mathrm{APF}}(r,t)\rangle_r = \partial_z p_{\mathrm{APF}}(t)\langle w_{\mathrm{APF}}(r)\rangle_r \\ =& -\tfrac{\partial_z p_{S,\mathrm{APF}}}{8}\tfrac{1-b^2+(1+b^2)\ln b}{(1-b)^2\ln b} - \tfrac{\partial_z p_{M,\mathrm{APF}}\sin(\Omega_{Re}t)}{8}\tfrac{1-b^2+(1+b^2)\ln b}{(1-b)^2\ln b} \\ =& \quad Re_S + Re_M \sin(\Omega_{Re} t), \end{aligned} \tag{4}$$

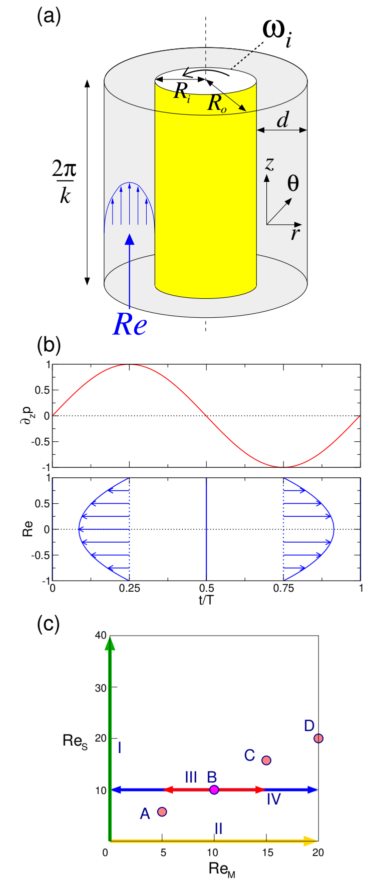

FIG. 1. (a) Schematic representation of the Taylor-Couette system to illustrate the (static) axial flow in an inner cylinder rotating configuration with a sketch of the laminar velocity profile $v(r,\theta)$ (not to scale). The imposed axial mass flux Re is considered positive from bottom to top. (b) Schematic representation of the pressure gradient (Eq. (2)) and the alternating velocity profile (axial Reynolds number $Re(t)$) as a function of time (normalized over a period). (c) Arrows I and II indicate the parameter space under investigation, which is spanned by $Re_S \in [0, 40]$ and $Re_M \in [0, 20]$. The explored parameter range in oscillating frequency spans $2\times10^{-3} \leqslant \Omega_H \leqslant 10^3$. Points A–D indicate the parameters for supercritical flows at $\mathrm{Re_i} = 100$. III and IV correspond to the set of parameters around the onset of stability for TVF in point B at $\mathrm{Re_i} = 73$.

with the three control parameters: Re_S is the *static contribution*, Re_M is the *modulation amplitude*, and Ω_{Re} is the *modulation frequency*. $Re(t)$ quantifies the additional axial pressure gradient applied externally. Therefore, a positive [negative] $Re(t)$ indicates an upward [downward] axial flow, $w_{\mathrm{APF}}(r,t)$, in the positive [negative] z-direction (see Fig. 1(b)). This implies that an axial flow can be characterized by the axial Reynolds number $Re(t)$ (Eq. (4)). Thus, positive Re favors [unfavors] L1-SPI [R1-SPI], as it is aligned [opposite] with the natural axial propagation of this flow structure.

In the present study, the system is identified as subcritical when for given system parameters only the basic state – here the CCF if $Re = 0$ or a combined circular Couette + annular Poiseuille flow (CCF-APF) if $Re \neq 0$ – is present in the system. On the other hand, supercritical indicates that at least one non-trivial solution solution exists, apart from the CCF (CCF-APF) basic state.

C. Symmetries

The governing equations and boundary conditions are invariant under arbitrary rotations R_α around the axis, arbitrary axial translation Z_l, and with respect to temporal translations ϕ_{t_0}. The effects of these symmetries on the velocity field are

$$R_\alpha(u,v,w)(r,\theta,z,t) = (u,v,w)(r,\theta+\alpha,z,t), \tag{5a}$$
$$Z_l(u,v,w)(r,\theta,z,t) = (u,v,w)(r,\theta,z+l,t), \tag{5b}$$
$$\phi_{t_0}(u,v,w)(r,\theta,z,t) = (u,v,w)(r,\theta,z,t+t_0). \tag{5c}$$

These idealizations lead to the CCF as the unique basic state, which depends only on r. The system has $SO(2)\times O(2)$ symmetry, where $SO(2)$ is the group of arbitrary rotations around the axis and $O(2)$ is the group that contains the reflection at arbitrary height z along with translations in z. The mean axial flux, which may be zero, remains unchanged along the radial direction and all symmetries (Eq. (5)) are preserved. For a finite axial flow $Re \neq 0$, the symmetry is invariant when switching between the two degenerate spiral vortex flows (left- and right-handed, L1-SPI and R1-SPI) along with the inversion of the axial flow direction of Re_S:

$$\text{L1-SPI}(Re_S,\alpha) = \text{R1-SPI}(-Re_S,\alpha). \tag{6}$$

The system symmetry with respect to Re_S is clearly visible in Fig. 2.

D. Numerical method

The Navier-Stokes equations (Eq. (1)) are solved using a second-order time-splitting method with consistent boundary conditions for the pressure[33,34]. Our code G1D3[36] is a combination of a finite-difference method in the radial and axial directions (r,z) and a Fourier-Galerkin expansion in the azimuthal direction (θ) with time splitting, which leads to the following decomposition

$$f(r,\theta,z,t) = \sum_m f_m(r,z,t)\, e^{im\theta} \tag{7}$$

of all fields $f \in \{u,v,w,p\}$. In this study, only axial periodic boundary conditions are considered. Here, we selected $m_{max} = 10$ (where m is the azimuthal wavenumber) to provide reasonable accuracy for the parameter range and flow structures under consideration. Further, uniform grid with a spacing $\delta r = \delta z = 0.02$ and time steps $\delta t < 1/3800$ is considered. A forward Time, centered space (FTCS) algorithm[37] is utilized to solve the system of coupled equations for the amplitudes $f_m(r,z,t)$ of the azimuthal normal modes $-m_{\max} \leqslant m \leqslant m_{\max}$. Further, the method of "artificial compressibility"[38] is considered for iteratively adjustment of pressure and velocity fields with respect to each other.

$$\begin{aligned} dp^{(n)} &= -\beta\nabla\cdot\mathbf{u}^{(n)} \quad (0<\beta<1),\\ p^{(n+1)} &= p^{(n)} + dp^{(n)},\\ \mathbf{u}^{(n+1)} &= \mathbf{u}^{(n)} - \Delta t\nabla(dp^{(n)}). \end{aligned} \tag{8}$$

The pressure correction $dp^{(n)}$ in the nth iteration step being proportional to the divergence of $\mathbf{u}^{(n)}$ is utilized to adapt the velocity field $\mathbf{u}^{(n+1)}$. In addition, the iteration loop (Eq. 8) is separately executed for each azimuthal Fourier mode. It is iterated until $\nabla\cdot\mathbf{u}$ becomes sufficiently small for each m mode considered – the magnitude of the total divergence never exceeded 0.02 and was typically much smaller. Time steps were always well below the von Neumann stability criterion and by more than a factor of three below the Courant-Friederichs-Lewy criterion. Hereafter, the next FTCS time step is executed.

For diagnostic purposes, we also evaluate the complex mode amplitudes $f_{m,n}(r,t)$, which we obtain from a Fourier decomposition in the axial direction

$$f_m(r,z,t) = \sum_n f_{m,n}(r,t)\, e^{inkz}. \tag{9}$$

E. Parameter setting and quantities

The parameter space explored in this study lies between $Re_S \in [-40,40]$ and $Re_M \in [-20,20]$. Further, we keep the outer cylinder at rest and investigate the effects of the time-dependent axial flow $Re(t)$ on the dynamics of the different flow states. Trajectories I and II depicted in the parameter space of Fig. 1(c) represent a purely static Re_S and a purely alternating axial Re_M flow, respectively. Points A–D depict the parameters for supercritical flows (TVF and SPI) at $\mathrm{Re_i} = 100$. Further, trajectories III and IV highlight the parameters where we perform a more detailed investigation around the onset of instability for TVF at point B and $\mathrm{Re_i} = 73$.

Flow states are characterized by the modal kinetic energy E_{kin} as a global measure:

$$E_{kin} = \sum_m E_m = \frac{1}{2}\int_0^{2\pi}\int_0^{\lambda}\int_{r_i}^{r_o} \mathbf{u}_m\mathbf{u}_m^* r\,\mathrm{d}r\,\mathrm{d}z\,\mathrm{d}\theta, \tag{10}$$

where $\mathbf{u}_m$ ($\mathbf{u}_m^*$) is the m-th (complex conjugate) Fourier mode, Eq. (7), of the velocity field. Thus, in case of axisymmetric solutions ($m = 0$)– for example CCF and TVF, only E_0 is non-zero. It must be noted that CCF and TVF are both pure $m = 0$ solutions and, therefore, an additional parameter – for example velocity profile – is required to be able to distinguish between them. If necessary, we consider the time-averaged quantity (over a period T) $\overline{E}_{kin} = \int_0^T E_{kin} \mathrm{d}t$ and the time-averaged mode amplitudes $\overline{|u_{m,n}|}$. Note that the period time of a particular solution was considered when investigating time-averaged quantities. Therefore, the period time of a solution depends on the parameters of a system, which are typically, different for different flow structures. As a local measure to characterize flow states, we also consider the azimuthal vorticity, $\eta = \partial_z u - \partial_r w$, on the inner cylinder and at mid-gap at two symmetrically displaced points on the mid-plane – $\eta_{-[+]} = (r_i, 0, \Gamma/4[3\Gamma/4], t)$.

III. RESULTS

A. Stability behavior

1. *Static axial through-flow* ($Re_M = 0$)

a. Supercritical flow states: Let us quickly review the case of a fully static axial flow Re_S ($Re_M = 0$) for a fixed inner Reynolds number, $\mathrm{Re_i} = 100$ (Fig. 2, outer cylinder at rest), before moving on to an external modulated axial flow. For the parameters given here, the different solutions – TVF, L1-SPI, and R1-SPI – partially stably coexist; therefore, the solution toward which the code will converge depends on the initial condition. Sitting in one stable solution, this branch is followed by variation in Re_S until the corresponding solution loses stability and transients into another remaining stable solution. For the various solutions TVF (blue circles), L1-SPI (orange triangles upwards), and R1-SPI (red triangles downwards), the variations in the kinetic energy E_{kin} (Eq. (10)) and the radial flow intensity (i.e., the amplitude of the radial mode, see Eq. (9)) in the center of the gap are displayed. These three flow configurations steadily coexist at $Re_S = 0$, with the two spirals, L1-SPI and R1-SPI, being mirror reflections of one another. Consequently, $|u_{1,1}| = |u_{1,-1}|$ and their respective axial velocities point in the *opposite* direction but have the same magnitude.

For any *finite* flow, $Re_S \neq 0$, the mirror symmetry between the L1-SPI and R1-SPI is *broken*, and as Fig. 2 illustrates, the radial flow amplitudes evolve differently with Re_S. For a minor flow rate of $-5.4 \lesssim Re_S \lesssim 5.4$, the two SPIs coexist and are bistable. In this case, the initial condition determines whether one or the other is realized. When Re_S increases, a shift in the phase velocity's sign (w_{ph} goes through zero) results in a loss of stability for either SPI[14,22]. Instead of transitioning to the remaining stable SPI state, the flow preferably transitions to the stable TVF state. Thus, when R1-SPI is destabilized with increasing Re_S, it is typically the $|u_{0,1}|$ mode of TVF that grows rather than the $|u_{1,1}|$ mode of L1-SPI. Moreover numerically eliminating the TVF solution (here, numerical suppressing $m = 0$ modes). The SPI that is unfavored by the through-flow Re loses its stability and in this case, the transition occurs (with TVF being unavailable as a final state) to the favored SPI in a manner that seems to be similar to the one described before. Moreover, for large values of $Re_S \gtrsim 30.3$ ($Re_S \lesssim -30.3$), TVF becomes unstable and the flow transitions toward the preferred spiral solution L1-SPI (R1-SPI). Thus, for given Re_S, the TVF solution does not exist; Consequently the system transitions to another stable solution – here SPI, which exists is for the new parameters.

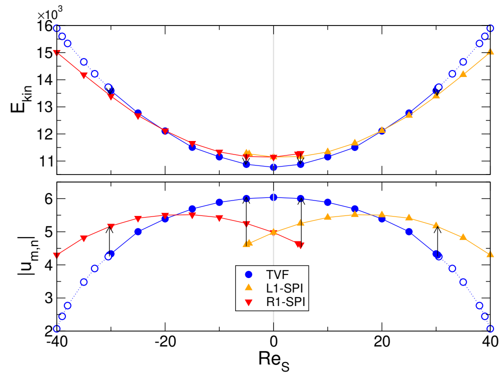

FIG. 2. Influence of the stationary external flow Re_S (see arrow I in Fig. 1(c)) on different vortex structures at $\mathrm{Re_i} = 100$. Shown are (top) the modal kinetic energy, E_{kin}, and (bottom) the primary Fourier amplitudes, $|u_{m,n}|$, of the radial flow field in the center of the gap $r = 0.5$ for L1-SPI ($u_{1,1}$), R1-SPI ($u_{1,-1}$), and TVF ($u_{0,1}$). Vertical arrows indicate transitions after loss of stability (see text for details). The unstable TVF solution is obtained by simulations restricted to the $m = 0$ subspace. Note the system symmetry with respect to static axial through-flow, Re_s (see Eq. (6)).

For TVF, an increase in $|Re_S|$ leads to a direct increase in E_{kin}. In contrast, for both L1-SPI and R1-SPI, an increase in $|Re_S|$ initially leads to a slight decrease in E_{kin} before it also increases for larger $|Re_S|$, which is to TVF but slightly less strong. Note, the system symmetry with respect to static axial through-flow, Re_s (Fig. 2 and Eq. (6)).

b. Shifting primary instabilities: Consider that a static axial flow ($Re_M = 0$) leads to the stabilization of the CCF basic state. Then, the bifurcation thresholds for primary instabilities, TVF and SPI, shift to larger $\mathrm{Re_i}$ with increasing flow strength Re_S (Fig. 3(a)). Note that only positive Re_S are shown for reasons of symmetry (Eq. (6)). Without axial flow – that is $Re = 0$ – the critical value for TVF is $\mathrm{Re_i}^{TVF} = 68.8$, while SPI is unstable in the beginning ($\mathrm{Re_i}^{SPI} = 72.3$[35]). We also performed a linear stability analysis of the combined CCF-APF state that revealed that the amplitudes of the L1[R1]-SPI solutions go to zero at the bifurcation threshold values of $Re_i(Re = 0) \approx 72.3$. In addition, the numerical solutions of the full nonlinear revealed, that both L1-SPI and R1-SPI are unstable close to this threshold. It is worth noting that other axial wavenumber (here set to $k = 3.927$) will lead to other critical Reynolds numbers. As is evident in Fig. 2, the axial flow favors helical SPIs[14,17,21,22] therefore, as Re_S increases, the primary stable appearing solution changes from TVF to SPI at $Re_S \approx 15$.

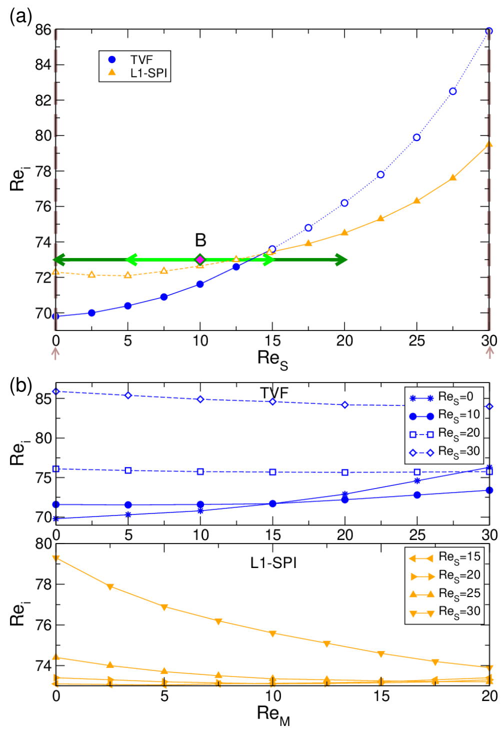

FIG. 3. Stability with axial flow. Stability limits for (a) static axial flow Re_S ($Re_M = 0$). Modulated axial flow Re_M vs. $\mathrm{Re_i}$ for (b) TVF and (c) SPI, respectively. Note that in (b) TVF is unstable for both $Re_S = 20$ and $Re_S = 30$, respectively. Vertical dashed lines in (a) indicate the parameters for which bifurcation diagrams are depicted in Fig. 4.

2. Modulated axial flow ($Re_M \neq 0$)

In comparison to the variation with increasing the flow strength, Re_S, for a pure static axial flow, an increase in the modulation amplitude, Re_M, has a more versatile effect on the system. For TVF and pure modulation flow ($Re_S = 0$), increasing the modulation amplitude Re_M also stabilizes the CCF basic state (Fig. 3(b)), with the bifurcation thresholds shifting to larger $\mathrm{Re_i}$. However, if a finite static contribution $Re_S \neq 0$ is present, the onset is only slightly affected. In addition, a small de-stabilization can be observed with increasing Re_M, which is most pronounced for larger Re_S. On the other hand, for SPI, the bifurcation thresholds are mainly shifted downward with increasing Re_M, thereby implying a de-stabilization of the CCF (Fig. 3(b)). This effect is most pronounced for $Re_S = 15$ and weakens with increasing static contribution, Re_S.

3. Bifurcation behavior

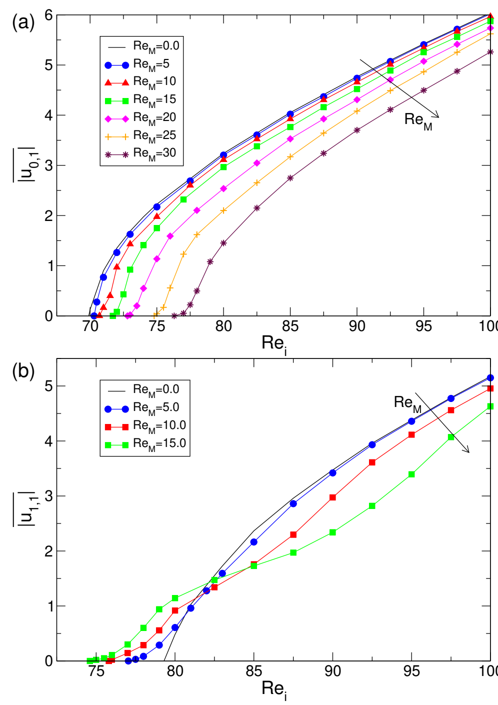

FIG. 4. Time-averaged mode amplitudes $\overline{|u_{0,1}|}$ and $\overline{|u_{1,1}|}$ of (dominant) radial flow field amplitudes of (a) TVF ($Re_S = 0$) and (b) SPI ($Re_S = 30$), respectively, at mid-gap as a function of the Reynolds number $\mathrm{Re_i}$ (parameters indicated by vertical dashed lines in Fig. 3); modulation frequency $\Omega_{Re} = 1$ (see Fig. 5). Note that the time average is identical for all curves (a) $\langle Re \rangle_t = 0$ and (b) $\langle Re \rangle_t = 30$.

Both TVF and SPI are primary bifurcating supercritical flow structures, with TVF occurring in a centrifugal instability and SPI in a symmetry-breaking Hopf bifurcation. However, with a finite modulation $Re_M \neq 0$, the corresponding approaches of TVF and SPI are blurred, which leads to the system appearing to be transient (between supercritical and subcritical) in a parameter range around the onset of bifurcation (Fig. 4). This fuzzy effect becomes larger with increasing Re_M as the parameter range increases with the transient behavior, which is visible in the tongue-like evolution of the mode amplitudes ($|u_{0,1}|$, $|u_{1,1}|$) close to the onset instead of a classical square root behavior[14,22,28,35]. While the effect is moderate for TVF, it is much stronger for SPI and, furthermore, a general change in the bifurcation behavior can be observed. With increasing Re_M, the the corresponding curves $|u_{1,1}|$ become flatter and more indented.

B. Nonlinear dynamic system response

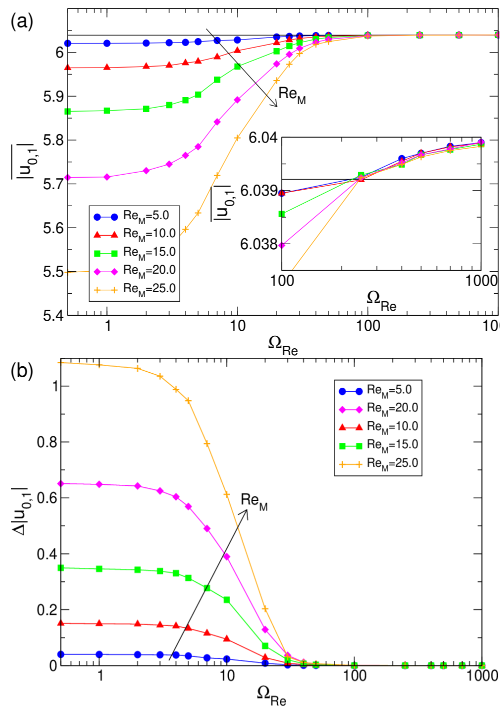

FIG. 5. Influence of the modulation frequency Ω_{Re} on the flow dynamics of the TVF at $\mathrm{Re_i} = 100$. Mode variation (a) $|u_{0,1}|$ and mode amplitude variation (b) $\Delta|u_{0,1}| = \max|u_{0,1}| - \min|u_{0,1}|$ with variation of the drive frequency Ω_{Re}.

Figure 5 illustrates the influence of the modulation frequency Ω_{Re} on the flow dynamics at TVF ($\mathrm{Re_i} = 100$). For small Ω_{Re}, the average amplitudes of the modes $|\overline{u}_{0,1}|$ are smaller compared to the modes $|u_{0,1}|$ for the scenario in which there is an absence of any axial flow, $Re = 0$. Here, the reduction becomes larger with increasing modulation amplitude Re_M, which is consistent with the stabilization of the CCF basic state and the shift of the primary bifurcation threshold to larger control parameters (see Fig. 3). With increasing Ω_{Re}, the average amplitudes of the modes $\overline{|u_{0,1}|}$ begin collapsing toward the corresponding mode $|u_{0,1}(Re = 0)|$ if no alternating axial flow is present – that is, no axial flow. Figure 5(b) provides another perspective of this collapse and illustrates the mode amplitude variation $\Delta|u_{0,1}| = \max|u_{0,1}| - \min|u_{0,1}|$. Therefore, in the limit range of high frequencies, only the mean value is significant. Interestingly, for very high frequencies, $\Omega_{Re} \gtrsim 250$, the average amplitudes of the modes $\overline{|u_{0,1}|}$ are slightly larger than even the one for the static case (see inset Fig. 5(a)). Further investigations are required to understand this observation and to draw any conclusion.

1. Supercritical flow states

In the following account, we consider supercritical flow states, TVF and SPI at $\mathrm{Re_i} = 100$ (far away from the onset of their respective instabilities ($\mathrm{Re_i}^{TVF}(Re = 0) = 68.8$) and $\mathrm{Re_i}^{SPI}(Re = 0) = 72.3$)[35]) and analyze the impact of an external superimposed alternating axial flow.

a. TVF: Figure 6 depicts the oscillation of the control function $Re(t)$ together with the non-linear system response, illustrated by the mode amplitudes $|u_{0,1}|$ as a function of the reduced time t/T_{Re} ($T_{Re} = 2\pi/\Omega_{Re}$ being the associated modulation period). Temporal oscillations are presented for $Re_S = Re_M \in \{5, 10, 15, 20\}$ at different frequencies Ω_{Re}, as depicted.

The results for different modulation amplitudes Re_M are qualitatively similar. In the high-frequency limit (red dashed lines in Fig. 6), only the time average of $Re(t)$ affects the stability behavior in this limit, the stability boundary coincides with a static stability boundary using an equivalent static axial flow, Re_S, which is equivalent to the corresponding mean value $\langle Re_S \rangle_t \in \{5, 10, 15, 20\}$ (values indicated in each subplot). For the modulation with the high frequency $\Omega_{Re} = 100$, the flow dynamics is basically averaged (also see Fig. 5) and variations in the dominant mode amplitude $|u_{0,1}|$ are small compared to its mean value. To be precise, the modulation amplitude $\Delta|u_{0,1}|$ is much less than 1% of its time mean. However, a phase shift is found between the maximum and minimum of $Re(t)$ (a) versus the minimum and maximum of the mode amplitudes $|u_{0,1}|$ $(b - e)$, with the inertia of the fluid leading to this time lag. Consistently, this phase shift decreases with decreasing frequency. Meanwhile, the oscillation amplitudes increase with smaller Ω_{Re} and by lowering the modulation frequency, thereby approaching the corresponding values (dotted horizontal lines) for a pure static axial flow curve. It is worth noting that small deviations persist in the vicinity of the bifurcation threshold as the dynamics become infinitely slow there.

As one approaches the static limit, the strong anharmonic behavior in the mode amplitudes $|u_{0,1}|$ for very low frequencies illustrates how the effect on the flow dynamics increases as $Re(t)$ increases. The stabilization effect is non-linear and stronger for a larger modulation amplitude, Re_M, as illustrated in Fig. 3. This fact is depicted in Fig. 6, in which the positive modulation amplitude $Re_M > Re_S$ has a steeper or larger variation $\Delta|u_{0,1}|$, and the negative modulation amplitude $Re_M < Re_S$ has a considerably flatter profile $|u_{0,1}|$.

The mode amplitudes $|u_{0,1}|$, within one period, somewhat overshoot the maximum and lowest values of their static counterparts at low frequencies, Ω_{Re}, approaching the static situation. For $\Omega_{Re} \in \{2, 5\}$, this overshoot is evident, and it is particularly noticeable around $Re_{m,max}$ for $t/T_{Re} \approx 0.25$. The mode amplitudes $|u_{0,1}|$ wander around the average well within their maximum and lowest bounds for high frequencies, $\Omega_{Re} \gtrsim 20$. This overshooting is brought on by the fluid's inherent inertia.

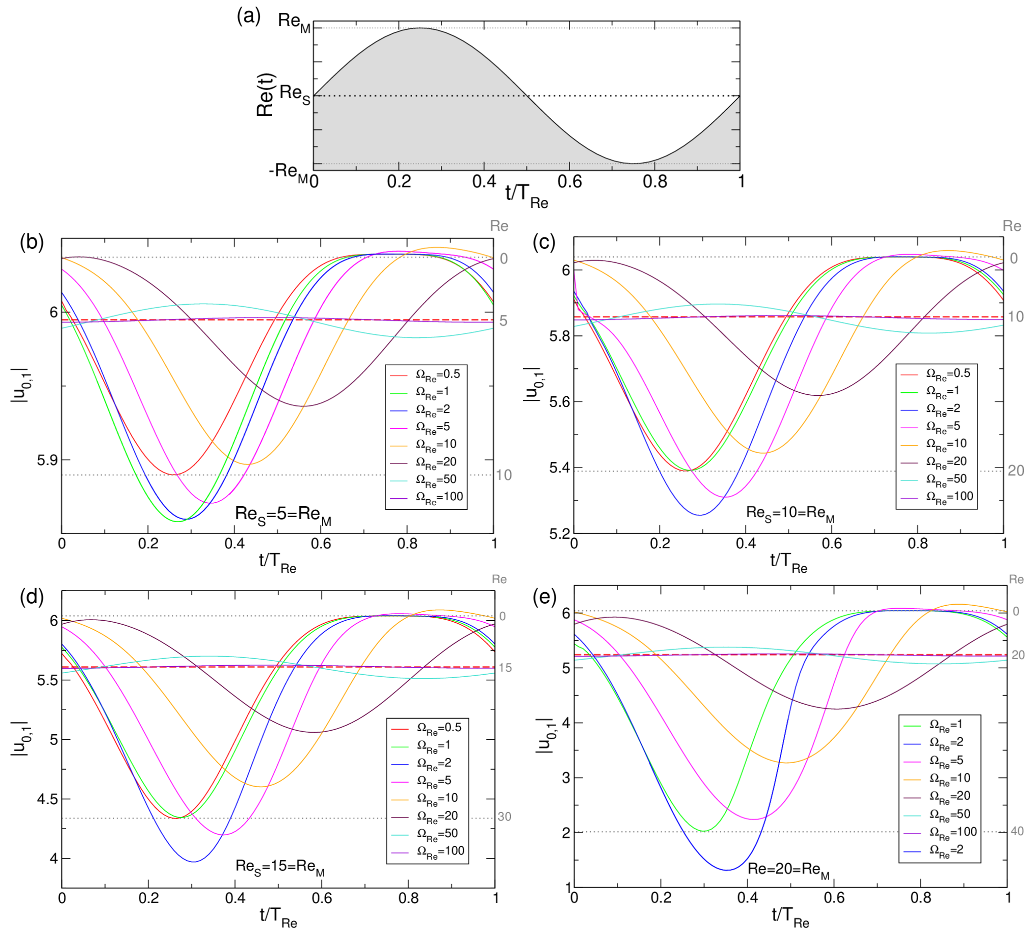

FIG. 6. Supercritical TVF under alternating axial flow $Re(t)$ with different driving frequencies Ω_{Re}. (a) Temporal oscillations of the control function $Re(t) = Re_S + Re_M \sin(\Omega_{Re} t)$ (Eq. (4)). The dominant mode amplitude $|u_{0,1}|$ as a function of the reduced time $t/T_{Re}(T_{Re} = 2\pi/\Omega_{Re}$ being the modulation period associated with the corresponding frequency) for parameter values (b) $Re_S = 5 = Re_M$; (c) $Re_S = 10 = Re_M$; (d) $Re_S = 15 = Re_M$; and (e) $Re_S = 20 = Re_M$, respectively, are displayed (see Fig. 1(c)). Horizontal dotted lines indicate the high frequency limit which is equivalent to stationary driving with corresponding mean values Re_S. The horizontal gray dotted lines indicate the corresponding minima ($min[Re(t)]$) and maxima ($max[Re(t)]$), respectively ($\mathrm{Re_i} = 100$). Note the different scaling on the ordinate; moreover, for (e) $Re_S = 20 = Re_M$ and $\Omega_{Re} = 0.5$, no curve is depicted as TVF becomes unstable. Here, the system transitions to the SPI solution and remains there.

b. SPI: As predicted in Fig. 3, increasing Re_M mainly destabilizes the CCF basic state against SPI. As Fig. 7 illustrates, the entire flow dynamics appear more complicated for SPI than for TVF. As seen for TVF (Fig. 6) and SPI in the high frequency limit, only the average values are of significance. A further common observation is the appearance of overshooting of the corresponding stationary values, which become enlarged with increasing modulation amplitude, Re_M. Further, at larger parameter $Re_S = Re_M \in \{10, 15, 20\}$ (Fig. 7$(c-e)$), the profiles of the mode amplitudes $|u_{1,1}|$ undergo significant change. For small values, $Re_S = 5 = Re_M$ (Fig. 7(b)), the profiles for SPI are qualitatively similar compared to the profiles of TVF (Fig. 6) in the sense that they illustrate one maximum and one minimum value within a single oscillation period T_{Re}. However, this similarity is lost for larger parameters $Re_S = Re_M$ (Fig. 7$(c-e)$) with the appearance of two minima and maxima, respectively, within one period, T_{Re}. Interestingly, the appearance of the two minima in time coincide with

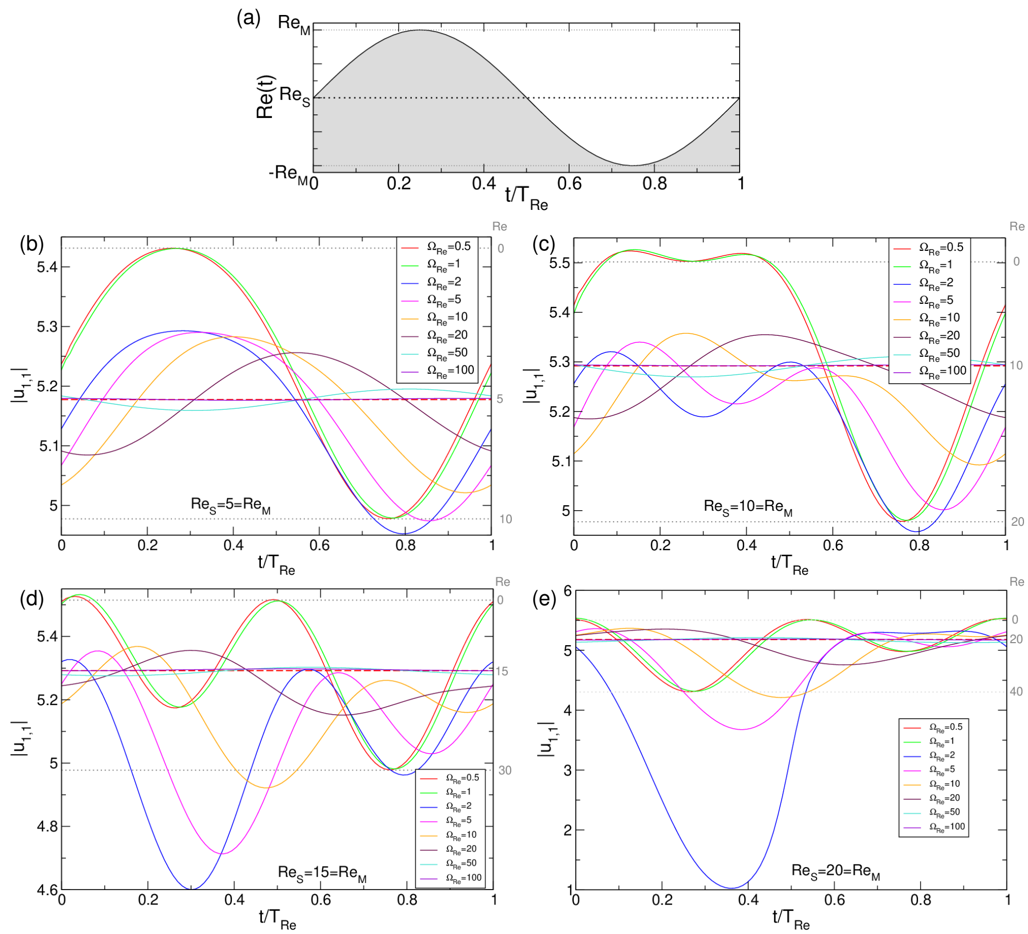

FIG. 7. This is similar to Fig. 6, but depicts supercritical SPI under alternating axial flow $Re(t)$ with different driving frequencies Ω_{Re} at (b) $Re_S = 5 = Re_M$; (c) $Re_S = 10 = Re_M$; (d) $Re_S = 15 = Re_M$; and (e) $Re_S = 20 = Re_M$, respectively ($\mathrm{Re_i} = 100$).

the presence of two vortices within the bulk side-by-side in radial direction. However, thus far, we have been unable to find a direct correlation, further investigations in this regard are required. It is worth mentioning that these are not similar to the known twin-vortices, which commonly have $m = 0$ and therefore, have azimuthal closed structures and originate in a different way. Here, the cause of appearance is different. First, SPI are already natural helical structures that also propagate in the axial direction, which can be enforced, reduced, or suppressed by axial flow Re depending on its direction[14,22] – second, here only the inner cylinder is driven (outer cylinder at rest). For lower frequencies and due to the inertia of the fluid (only driven from the inner cylinder), this results in the formation of this second vortex in the radial direction.

2. Nonlinear system response – crossing the primary instability

Next, we concentrate on an alternating axial flow for values, such that, over a driving period (see Fig. 3(a)), the system will transition between subcritical and supercritical responses. Specifically, we take into account $\mathrm{Re_i} = 73$ and an alternating axial flow with two distinct modulation amplitudes, $Re_M = 5$ and $Re_M = 10$, respectively, and a fixed stationary contribution, $Re_S = 10$. With regard to the pure static case, the system becomes temporally subcritical for both modulation amplitudes considered, Re_M, but it is totally supercritical (see point B in Figs. 1 and 3(a)).

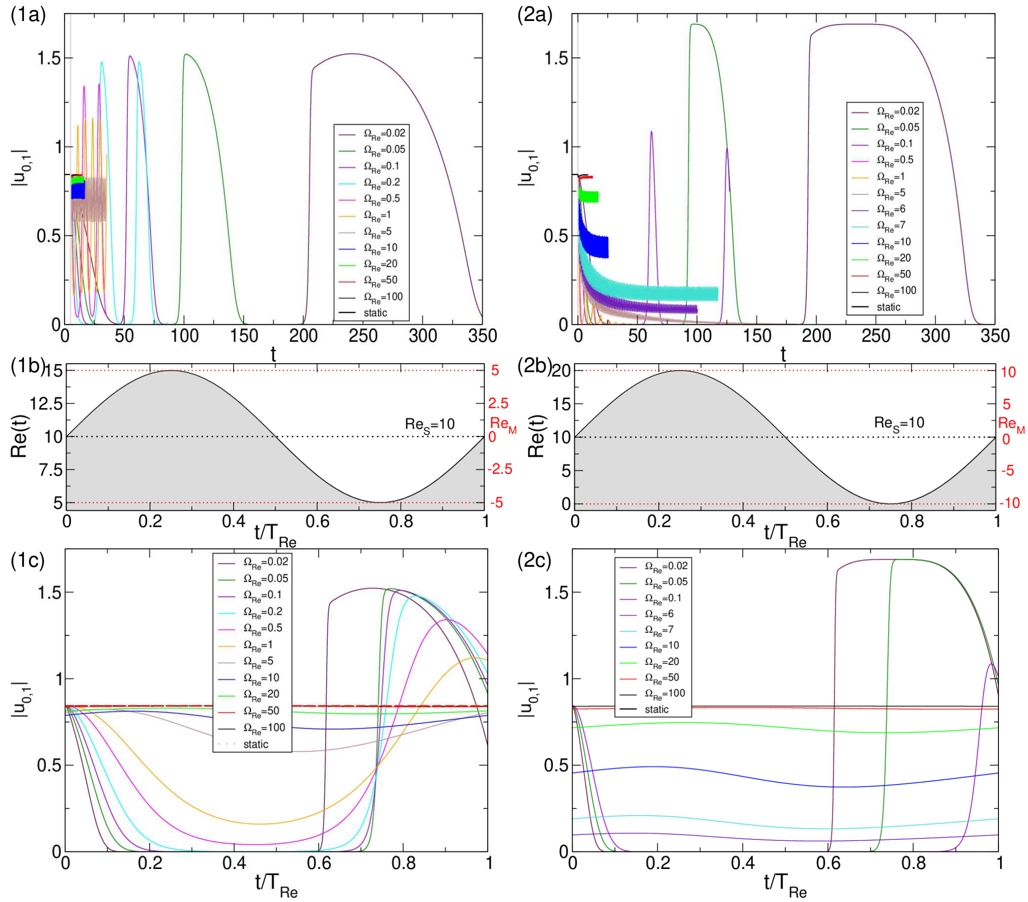

FIG. 8. Nonlinear system response of TVF around the fundamental instability. (a) Time evolution of the modulation amplitudes (1) $Re_M = 5$ and (2) $Re_M = 10$, respectively, and the dominant mode amplitude $|u_{0,1}|$ as a function of time, t, for various modulation frequency, Ω_{Re}, as indicated (see trajectories III and IV in Fig. 1). At $t = 0$, only a static axial flow $Re_S = 10$ ($Re_M = 0$) is present before any of these modulations begins. For larger frequencies, Ω_{Re}, the mode amplitudes, $|u_{0,1}|$, are only displayed until equilibrium is reached; for the sake of clarity, long time simulations have been carried out to confirm that these are all permanent states. For the lowest frequency ($\Omega_{Re} = 0.05$), a minimum of five repetitions were covered to ensure a permanent (and not transient) behavior. As a function of the reduced time t/T_{Re}, (c) is the same as (a) (see Fig. 7). Bear in mind that the system is still supercritical in (1) for modulated driving with $\Omega_{Re} \gtrsim 0.45$. Apart from (2), the system remains supercritical for large driving with $\Omega_{Re} \gtrsim 5.6$. However, it remains subcritical for moderate modulated driving with $5.6 \gtrsim \Omega_{Re} \gtrsim 0.2$, and it alternates between subcritical and supercritical response for small driving with $0.2 \gtrsim \Omega_{Re}$. Furthermore, within a narrow parameter range of $0.08 \lesssim Re_\Omega \lesssim 0.12$, the system exhibits irregular intermittent behavior (see Figs. 10 and 11 for details). Further control parameter is $\mathrm{Re_i} = 73$.

a. Small modulation amplitude ($Re_M = 5$). In this case, the system only briefly approaches subcriticality. The time averaged axial flow $\langle Re \rangle_t$ for modulated driving (dashed red line in Fig. 8($1a, 1c$)) comes together with the static case $Re_S = 10$ ($Re_M = 0$) at a high frequency limit ($\Omega_{Re} \gtrsim 100$). The oscillating mode amplitude $|u_{0,1}|$ experiences a continuous increase in amplitude $|\Delta u_{0,1}|$ with decreasing frequency Ω_Re, accompanied by a reduction in its mean value $|\overline{u}_{0,1}|$. The mode amplitude $|u_{0,1}|$ eventually approaches temporally zero for frequencies $\Omega_{Re} \lesssim 0.25$, thereby suggesting that the system is now *subcritical*. The smaller the driving frequency, Ω_{Re}, the longer the system remains subcritical (Fig. 8($1c$)).

At these low frequencies, the mode amplitude $|u_{0,1}|$ rapidly increases during a period and then relaxes in a manner that is

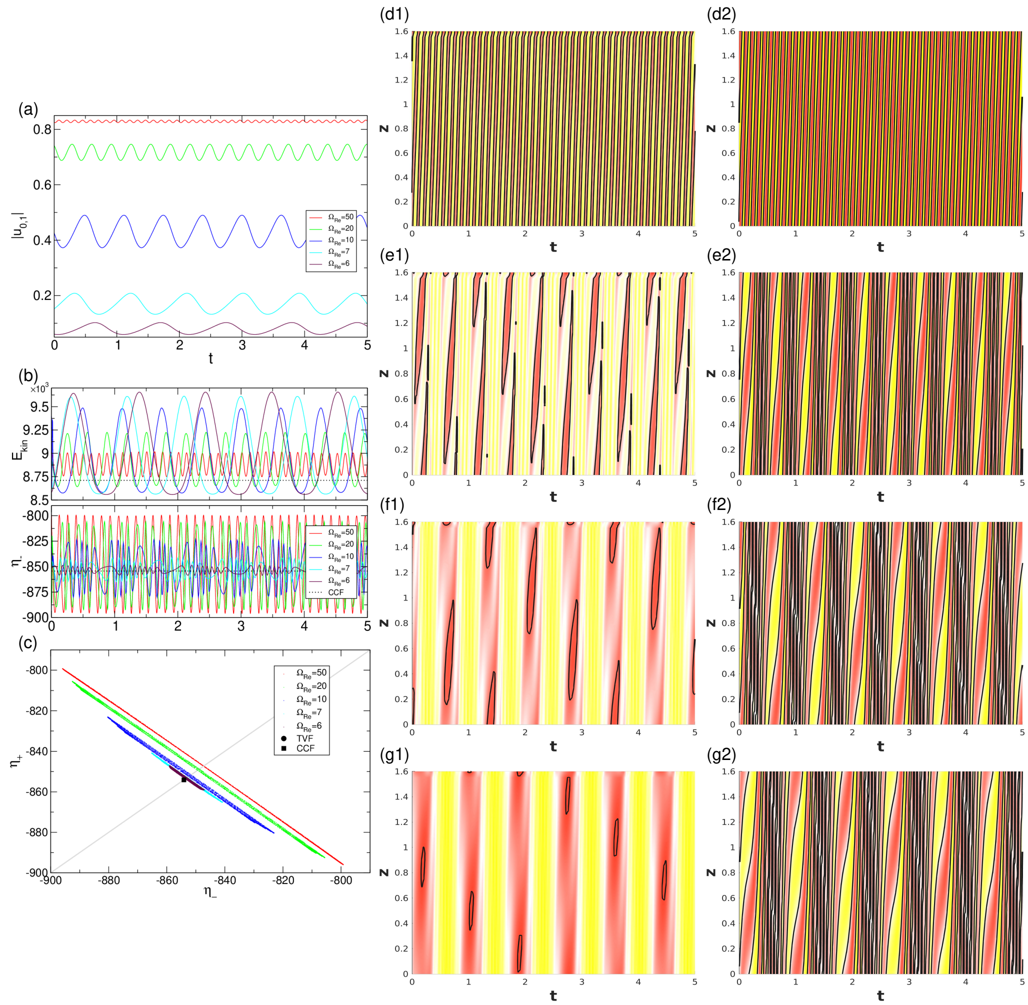

FIG. 9. Flow dynamics with time t for stable TVF with driving frequencies Ω_{Re} for $Re_S = 10$ and $Re_M = 10$, as shown. Time evolution of the radial velocity field at mid-gap and (b) kinetic energy E_{kin} and η_-, representing the dominant mode amplitudes $|u_0,1|$ (see Eq. (9)). (c) Corresponding phase portrait in (η_+,η_-) plane (see text for more discussion). $(c)-(f)$ Azimuthal vorticity space-time plots η (1) $\eta(z=0,\theta=0,r=d/2)$ and the radial speed (2) $u(z=0,\theta=0,r=d/2)$ for various frequencies, (red denotes dark grey and yellow denotes light grey) correspond to positive and negative numbers, respectively. Specifically, (d) $\Omega_{Re}=0.2$; (e) $\Omega_{Re}=0.5$; (f) $\Omega_{Re}=1$; and (g) $\Omega_{Re}=2$.

similar to values that are close to the stationary case. The oscillation profile in the mode amplitudes $|u_{0,1}|$ approaches the static scenario when Ω_{Re} decreases further. The situation for the entire supercritical flow state (Fig. 6) and the accompanying extrema (min and max) in the mode amplitudes $|u_{0,1}|$ are shown to be temporally induced separate from one another.

b. Large modulation amplitude ($Re_M = 10$). The initial response is comparable to the case for the small modulation amplitude when the system delves deeper into the subcritical regime for a larger modulation amplitude, $Re_M = 10$ (see Fig. 3(a)), during one driving period (Fig. 8(2)). With the time-averaged axial flow $\langle Re\rangle_t$ (dashed red line in Fig. 8(2c)), which is equal to the static case, $Re_S = 10$ ($Re_M = 0$), the

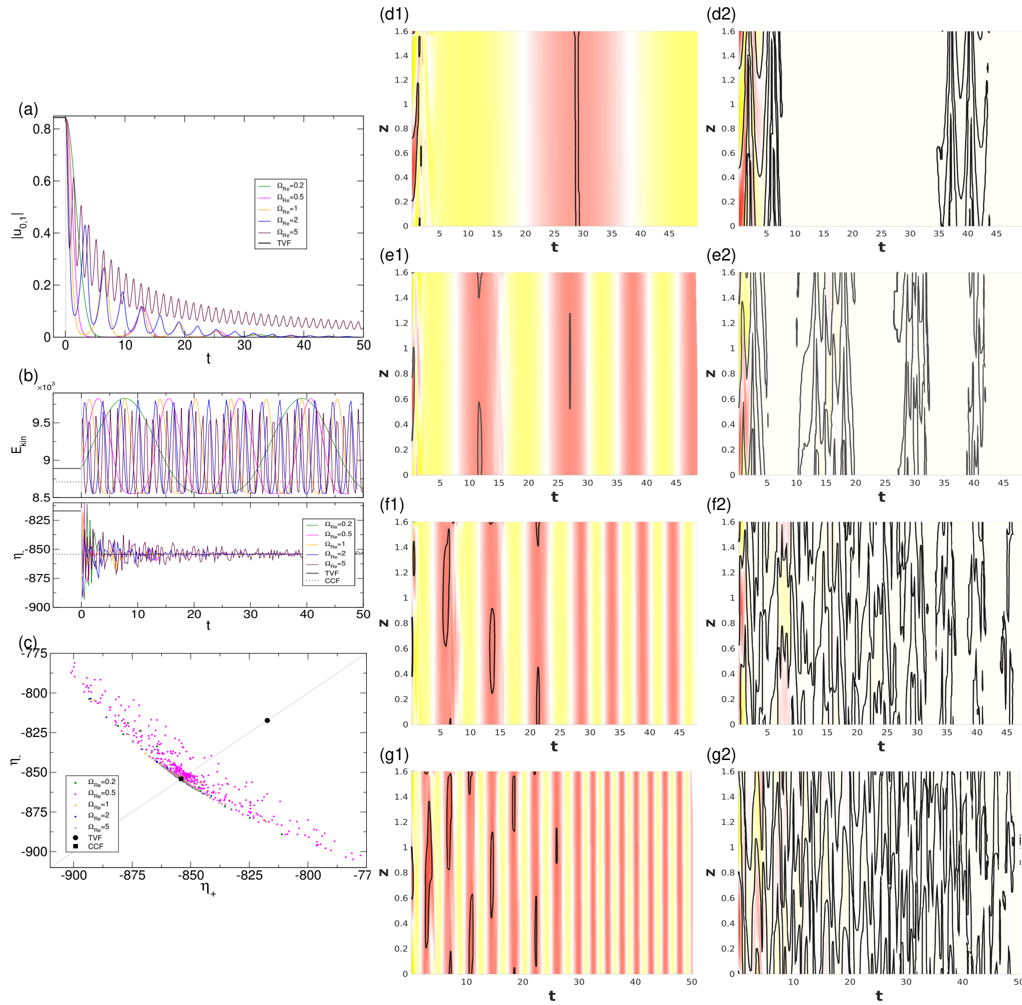

FIG. 10. The flow dynamics during the TVF decay for $Re_S = 10, Re_M = 10$ with driving frequencies Ω_{Re} (see Figs. 9 and 8). (d) $\Omega_{Re} = 0.2$, (e) $\Omega_{Re} = 0.5$, (f) $\Omega_{Re} = 1$, and (g) $\Omega_{Re} = 2$.

system remains supercritical in the high frequency limit. Nevertheless, there are a few obvious distinctions, despite this resemblance. First, there is a discontinuity in the modulation of the mode amplitude $|\Delta u_{0,1}|$; in other words, it remains relatively small and of a comparable size. Second, when Ω_{Re} decreases, the mean values $|\overline{u}_{0,1}|$ also constantly reduce. Furthermore, the system remains completely subcritical for a limited range with modulated driving. With regard to modest modulation amplitude (Fig. 8(1)), this is a novel observation that has not been discovered thus far. The subcriticality for the given alternating flow is clearly evident in the decay of the mode amplitudes $|u_{0,1}|$ in Fig. 8($2a$) for modulated driving with $5.6 \gtrsim \Omega_{Re} \gtrsim 0.2$. Nevertheless, as previously observed for modest modulation magnitudes, this permanent subcritical behavior reverts to being merely temporal with additional decreases in Ω_{Re}. Consequently, a temporal fluctuation between subcritical and supercritical system reactions is observed once more. Similar to the previous observation, there is a rapid increase in the mode amplitude $|u_{0,1}|$, which is followed by a relaxation towards the stationary state. The oscillation increases with a decrease in the modulation frequency Ω_{Re}. Minor variations in the frequency of the instability and driving frequency Ω_{Re} may be the result of resonance effects. Further investigations are required in order to make a conclusive statement.

Stable, supercritical TVF. The flow dynamics evolving with time t for specific driving frequencies Ω_{Re} (at $Re_S = 10 = Re_M$) are depicted in Figure 9; at these frequencies, TVF are stable existent; the system remains permanently supercritical (see Fig. 8(2)). The variation in ΔE_{kin} grows constantly with decreasing Ω_{Re}, but the mean value $\overline{E}_{kin}$ mostly remains constant. Further, the mode amplitudes $|\overline{u}_{0,1}|$ have a monotonically decreasing mean in parallel. It is interesting to note that the mode amplitude variation, $|\Delta u_{0,1}|$, is non-monotonic – increasing initially and then reducing again. Concurrently, the local measure $\Delta\eta_-$ experiences a reduction in range, transitioning from a basic periodic behavior to a more intricate "multi-periodic" pattern (combining different periodicities). Consequently, with smaller frequencies, Ω_{Re}, the area explored by the trajectories in the phase portrait in the (η_+, η_-) plane constantly shrinks towards the CCF solution. In (η_-, η_+), the two stationary solutions, CCF and TVF, are fixed points. With regard to the diagonal line $\eta_- = \eta_+$, the (time-dependent) limit cycle solution TVF generated by the alternating flow ($\Omega_{Re} \neq 0$) appears symmetric. With variation in Ω_{Re}, the various space-time plots $(d-g)$ of the azimuthal vorticity η provide an additional qualitative sense of all the previously stated alterations.

Decay process. As previously noted, the system becomes permanently subcritical for modulated driving with $5.6 \gtrsim \Omega_{Re} \gtrsim 0.14$ at large modulation amplitudes, $Re_M = 10$ (Fig. 8(2)). The evolving flow dynamics that change with time t during TVF's decay are depicted in Fig. 10. Together with the space-time plots of the azimuthal vorticity $\eta_- = \eta(r = d/2, \theta = 0, z)$ and radial velocity $u(r = d/2, \theta = 0, z)$, (red (dark grey) and yellow (light grey) correspond to positive and negative values) for a selected frequency Ω_{Re}, the dominant mode amplitudes $|u_{0,1}|$ are displayed. The decay of TVF with time is evident in both mode amplitudes: η_- nearing the comparable value for CCF and $|u_{0,1}|$ dropping to zero. In the meantime, the region that the trajectories in the (η_+, η_-) plane have traversed become smaller and closer to the CCF fixed point solution.

c. Intermittency. The system response shifts from being permanently subcritical to alternating between subcritical and supercritical behavior with decreasing driving frequencies Ω_{Re}. The system exhibits a "regular" (time-periodic) intermittent behavior around the "edge" for $\Omega_{Re} \lesssim 0.07$, thereby implying that it alternates between the supercritical TVF state and the subcritical CCF state on a periodic basis. According to Fig. 8(2c), the system remains supercritical for a longer period of time, T_{Re}, the smaller the driving frequency Ω_{Re}. In the sense that the corresponding dwell/retention duration in the subcritical and supercritical regimes remains the same, the behavior is "regular" intermittent.

At low frequencies, $\Omega_{Re} \lesssim 0.07$, the system displays a regular intermittent behavior between subcritical and supercritical system response, as is evident for small modulation amplitudes $Re_M = 5$ (Fig. 8). However, around the transition from the permanent subcritical state CCF (TVF is unstable and decays) to the intermittent behavior between the two – subcritical and supercritical states – there is a narrow frequency range, $0.13 \gtrsim \Omega_{Re} \gtrsim 0.07$, in which the system response is "irregular" intermittent. Figure 11 depicts the mode amplitudes and space-time diagrams for selected frequencies, Ω_{Re}, at which the system shows this irregular intermittency. In contrast to the previously seen regular behavior, the system here has no fixed dwell time in one or the other regime. Therefore, the dwell time changes from one alternating cycle to the next. Both the mode amplitudes, $|u_{0,1}|$, and the azimuthal vorticity, η_-, clearly show the "irregularity", which is not recognizable in the kinetic energy E_{kin}. The phase portrait in the (η_+, η_-) plane appears rather similar to that for the decay of TVF (see Fig. 10), with the main difference being that the phase space explored by the trajectories is rather large. The corresponding 3D visualization with E_{kin} reveals a cone-shaped structure with the CCF fixed-point solution at its apex.

Finally, it is worth mentioning that the observed non-linear system response is similar to ferrofluidic Couette flow under an alternating magnetic field[39]. Thus, the specific focus for future research will be the study resonance effects due to alternating axial flow, similar to those found for the TVF of a ferrofluid under an alternating magnetic field[40].

IV. CONCLUSIONS

The impact of an externally imposed time-dependent axial mass flux (axial pressure gradient, axial through-flow $Re(t)$) in a wide-gap Taylor-Couette flow was qualitatively and quantitatively studied in this paper. TVF and SPI's primary instabilities are altered. They are shifted towards a larger control parameter, $\mathrm{Re_i}$, for TVF, where a larger modulation amplitude, Re_M, results in an increase in the stabilization amount. This alteration is comparable to that caused by only static axial through-flow when Re_S increases in terms of field strength. In the high-frequency limit, the system's temporal evolution approaches the static stability boundary as the oscillation frequency Ω_{Re} increases. The oscillation profiles become closer to the stationary curves at rather low modulation frequencies.

Moreover, we discovered that the system response is specific to driving parameters that were close to the main instability. Because of this, a system driven by an alternating axial mass flux might become subcritical or supercritical, or it can even alternate (regularly or irregularly intermittent) between the two states.

The non-linear system response based on small and large modulation amplitudes Re_M with respect to variation in the driving frequency Ω_{Re} is schematically summarized in Fig. 12. In any event, one solution – supercritical TVF – is selected as the high frequency limit gets closer to the static situation.

While hovering and straddling the edge of instability, the following key features can be characterized by changes in the driving frequency:

- When the frequency, Ω_{Re}, decreases and the modulation amplitudes are minimal, the system transitions from be-

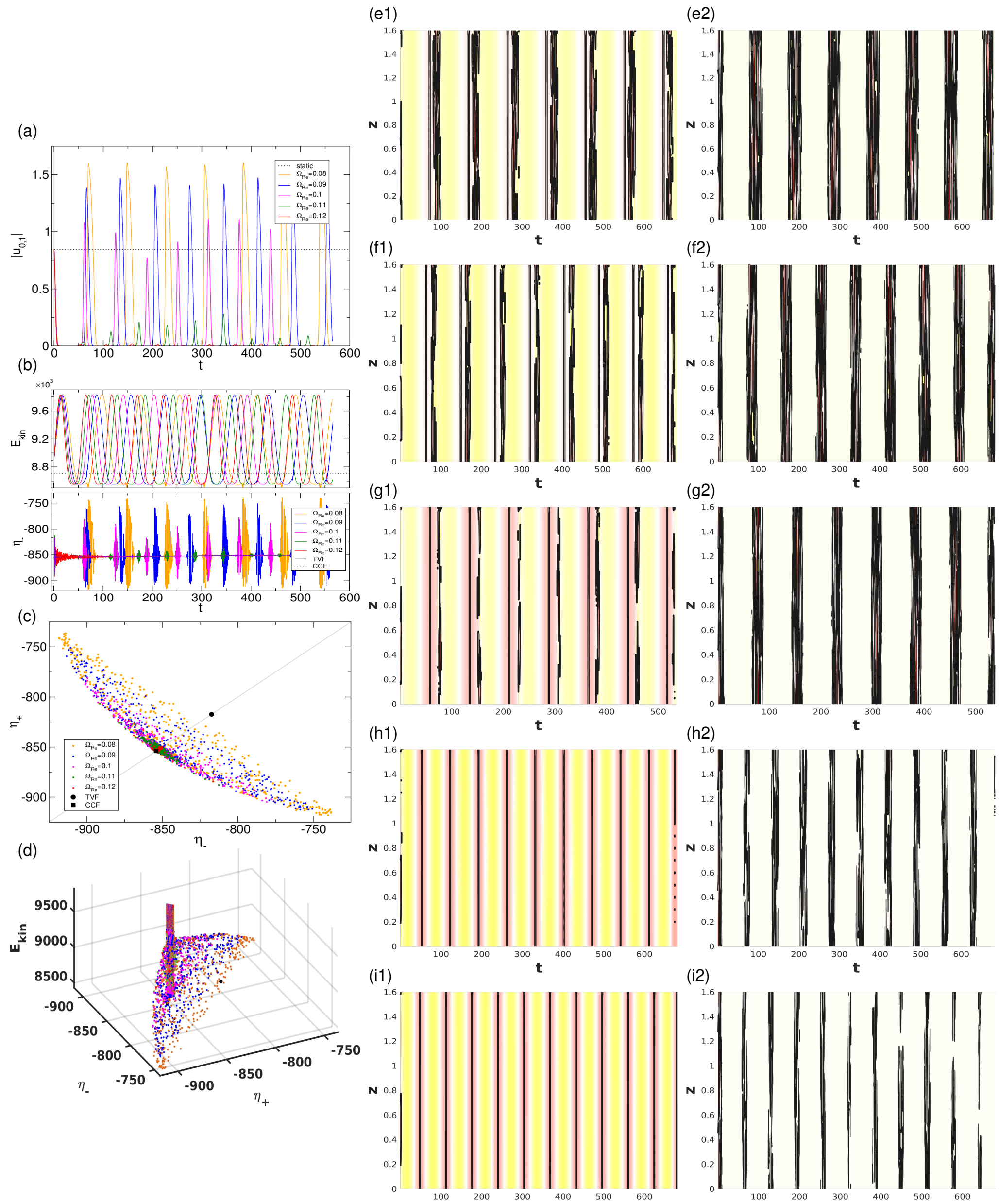

FIG. 11. Illustration of the dynamics of irregular, sporadic flow – irregular intermittent behavior of TVF for $Re_S = 10, Re_M = 10$ with driving frequencies Ω_{Re}, as indicated. Time evolution of (a) dominant mode amplitudes $|u_{0,1}|$ (see Eq. (9)) of the radial velocity field at mid-gap and (b) kinetic energy E_{kin} and η_-. (c) Corresponding phase portrait in (η_+, η_-) plane and (d) Three-dimensional visualization $(\eta_+, \eta_-, E_{kin})$. (e)–(i) Space-time plots of the azimuthal vorticity (1) $\eta(r = d/2, \theta = 0, z)$ and radial velocity (2) $u(r = d/2, \theta = 0, z)$ (red (dark gray) and yellow (light gray) correspond to positive and negative values) for different frequencies (e) $\Omega_{Re} = 0.08$, (f) $\Omega_{Re} = 0.09$, (g) $\Omega_{Re} = 0.1$, (h) $\Omega_{Re} = 0.11$, and (i) $\Omega_{Re} = 0.12$.

ing supercritical to an intermittent scenario in which it becomes both temporally sub- and supercritical.

- The system first transitions from being supercritical to permanent subcritical with large modulation amplitudes and decreasing frequency, Ω_{Re}. Therefore, the system response is altered to be both temporally subcritical and supercritical by further reducing the frequency Ω_{Re} (equivalent to modest modulation amplitudes). However, the system response is irregular in a limited frequency range of $0.12 \gtrsim \Omega_{Re} \gtrsim 0.08$, which is approximately the "edge" between pure subcritical and the alternating sub- and supercritical system response – *intermittency*.

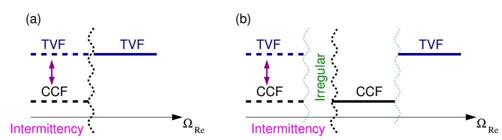

FIG. 12. Schematic representation of the change in stability with Ω_{Re}. As the driving frequency, Ω_{Re}, increases from left to right, the system transitions from exhibiting regular alternating behavior between sub- and supercritical flow states to supercritical TVF at small modulation amplitudes (a). The system exhibits alternating behavior between sub- and supercritical flow states for large modulation amplitudes (b) and increasing frequency. This is followed by irregular intermittency for a small range in Ω_{Re} and, finally, the system remains entirely subcritical (CCF). Nevertheless, at the high frequency limit analogue to the scenario with small modulation amplitude, the system becomes supercritical (TVF) again by increasing Ω_{Re} (see Fig. 8).

The findings of this paper, along with the spatio-temporal properties of vorticity fields and the velocity of various flow states, may open up new directions for the study of the transport properties of rotating flows. Therefore, the frequency modification of the alternating axial mass flux provides a rather simple and, importantly, precisely controllable method to induce subcritical or supercritical behavior in the system reaction. This could open up fresh avenues for and lead to the development of new viewpoints toward for industrial applications. Another important aspect that must be emphasized is the significant torque disparity that exists between the subcritical CCF basic states and the supercritical TVF basic states.

The system configuration and parameters that were discussed in this study are easily experimental accessible. Therefore, we hope that our computational results will encourage further experimental studies with the aim of studying transport phenomena and controlling flows with potential industrial applications – flow separation and filtration devices, oil-sand separation or extraction of blood plasma – just to mention a few.

ACKNOWLEDGMENTS

S. A. is a Serra Húnter Fellow. This work has been supported by the Spanish Government under grant number PID2019-105162RB-I00.

DATA AVAILABILITY STATEMENT

The data that support the findings of this study are available upon request from the corresponding author.

[1] G. I. Taylor, "Stability of a viscous liquid contained between two rotating cylinders", Philos. Trans. R. Soc. London A 223, 289 (1923).
[2] P. Chossat, and G. Iooss, "The Couette–Taylor Problem", Springer, Germany, Berlin (1994).
[3] B. Hallström, and M. Lopez-Leiva, "Description of a rotating ultrafiltration module", Desalination 24, 273 (1978).
[4] K. H. Kroner, and V. Nissinen, "Dynamic filtration of microbial suspension using an axially rotating filter", J. Membr. Sci. 36, 85 (1998).
[5] G. Belfort, J. M. Pimbley, A. Greiner, and K. Y. Chung "Diagnosis of membrane fouling using a rotating annular filter. 1. cell culture media", Membr. Sci. 77, 1 (1993).
[6] G. Belfort, J. M. Pimbley, A. Greiner, and K. Y. Chung, "Diagnosis of membrane fouling using a rotating annular filter. 2. dilute particule suspension of known particle size", J. Membr. Sci. 77, 23 (1993).
[7] S. T. Wereley, A. Akonur, and R. M. Lueptow, "Particle-fluid velocities and fouling in rotating filtration of a suspension", J. Membr. Sci. 209, 469 (2002).
[8] K. Ohashi, K. Tashiro, F. Kushiya, T. Matsumoto, S. Yoshida, M. Endo, T. Horio, K. Ozawa, and K. Sakai, "Rotation-induced Taylor vortex enhances filtrate flux in plasma separation", Trans. Am. Soc. Artif. Intern. Organs 34, 300 (1988).
[9] G. Beaudoin, and M. Y. Jaffrin, "Plasma filtration in couette flow membrane devices"; Artif. Organs 13, 43 (1989).
[10] R. M. Lueptow and A. Hajiloo, "Flow in a rotating membrane plasma separator", Trans. Am. Soc. Artif. Intern. Organs 41, 182 (1995).
[11] J. Yin, X. Liu, C. Zhou, and Z. Zhu, "Analysis and measurement of mixing flow field on side wall of large-scale mixing tank", Chem. Eng. 49, 73–78 (2021).
[12] J. Zhu, D. Liu, C. Tang, C. Q. Chao, and C. L. Wang, "Study of slit wall aspect ratio effect on the Taylor vortex flow", J. Eng. Thermophys. 37, 1208–1211 (2016).
[13] R. C. DiPrima, "The stability of a viscous fluid between rotating cylinders with an axial flow", J. Fluid Mech. 9, 621 (1960).
[14] Ch. Hoffmann, M. Lücke, and A. Pinter, "Spiral vortices and Taylor vortices in the annulus between rotating cylinders and the effect of an axial flow", Phys. Rev. E 69, 056309 (2004).
[15] D. Martinand, E. Serre, and R. M. Lueptow, "Absolute and convective instability of cylindrical Couette flow with axial and radial flows"; Phys. Fluids 21, 104102 (2009).
[16] D. Martinand, E. Serre, and R. M. Lueptow, "Linear and weakly nonlinear analyses of cylindrical Couette flow with axial and radial flows", J. Fluid Mech. 824, 438 (2017).
[17] S. T. Wereley and R. M. Lueptow "Velocity field for Taylor–Couette flow with an axial flow", Phys. Fluids 11 (12), 3637 (1999).
[18] A. Recktenwald, M. Lücke, and H. W. Müller, "Taylor vortex formation in axial throughflow: Linear and weakly nonlinear analysis", Phys. Rev. E 48, 4444 (1993).
[19] T. Gebhardt, and S. Crossmann, "The Taylor-Couette eigenvalue problem with independently rotating cylinders", Z. Phys. B: Condens. Matter 90 (4), 475–490 (1993).
[20] A. Mesegure, and F. Marquez, "On the competition between centrifugal and shear instability in spiral Poiseuille flow", J. Fluid Mech. 455, 129–148 (2002).
[21] A. Pinter, M. Lücke and Ch. Hoffmann, "Spiral and Taylor vortex fronts and pulses in axial throughflow", Phys. Rev. E 67, 026318, 1–15 (2003).

[22]S. Altmeyer, C. Hoffmann, and M. Lücke, "Islands of instability for growth of spiral vortices in the Taylor-Couette system with and without axial throughflow", Phys. Rev. E 84, 046308 (2011).
[23]R. Raffai, and P. Laure, "The influence of an axial mean flow on the Couette-Taylor problem", Eur. J. Mech. B/Fluids 12, 277 (1993).
[24]P. Büchel, M. Lücke, D. Roth, and R. Schmitz, "Pattern selection in the absolutely unstable regime as a nonlinear eigenvalue problem: Taylor vortices in axial flow", Phys. Rev. E 53, 4764–4777 (1996).
[25]J. B. Swift, K. L. Babcock, and P. C. Hohenberg, "Effects of thermal noise in Taylor-Couette flow with corotation and axial throughflow", Physica A 204, 625 (1994).
[26]R. J. Deissler, "Thermally sustained structure in convectively unstable systems", Phys. Rev. E 49 R31 (1994).
[27]A. Szprynger and M. Lücke, "Noise sensitivity of sub- and supercritically bifurcating patterns with group velocities close to the convective-absolute instability", Phys. Rev. E 67, 046301 (2003).
[28]N. Abchaa, O. Crumeyrolle, A. B. Ezerskya, and I. Mutabazi, "Velocity field of the spiral vortex flow in the Couette-Taylor system", Eur. Phys. J. E 36 20 (2013).
[29]S. Altmeyer and Y. Do, "Effects of an imposed axial flow on a Ferrofluidic Taylor-Couette flow", Scientific Reports 9, 15438 (2019).
[30]G. Baier and M. D. Graham, "Two-fluid Taylor-Couette flow with countercurrent axial flow: Linear theory for immiscible liquids between corotating cylinders", Phys. Fluids 12, 294-303 (2000).
[31]S. Chandrasekhar, "Hydrodynamic and hydromagnetic stability", Dover, New York, (1961).
[32]R. J. Leite "An experimental investigation of the stability of Poiseuille flow", J. Fluid Mech. 5, 81 (1959).
[33]S. Hughes and A. Randriamampianina, "An improved projection scheme applied to pseudospectral methods for the incompressible Navier Stokes equations", Int. J. Numer. Methods Fluids 28, 501 (1998).
[34]I. Mercader, O. Batiste, and A. Alonso, "An efficient spectral code for incompressible flows in cylindrical geometries", Comput. Fluids 39, 215 (2010).
[35]Ch. Hoffmann, S. Altmeyer, A. Pinter, and M. Lücke, "Transitions between Taylor vortices and spirals via wavy Taylor vortices and wavy spirals", New J. Phys. 11, 053002 (2009).
[36]S. Altmeyer, C. Hoffmann, M. Heise, J. Abshagen, A. Pinter, M. Lücke, and G. Pfister, "End wall effects on the transitions between Taylor vortices and spiral vortices", Phys. Rev. E 81, 066313 (2010).
[37]C. W. Hirt, B. D. Nichols, and N. C. Romero *SOLA-A Numerical Solution Algorithm for Transient Fluid Flow*. Los Alamos Scientific Laboratory of the University of California, LA-5852 (1975).
[38]R. Peyret and T. D. Taylor *Computational Methods in Fluid Flow*. Springer, Germany, Berlin (1983).
[39]S. Altmeyer, "On the ridge of instability in ferrofluidic Couette flow via alternating magnetic field", Scientific Reports 11, 4705 (2021).
[40]S. Altmeyer, "Ferrofluidic wavy Taylor vortices under alternating magnetic field", Phil. Trans. R. Soc. A 381, 20220121 (2023).